Crystal structure and local order of nanocrystalline zirconia-based solid solutions

I. O. Fábregas, D. G. Lamas, L. M. Acuña, and N. E. Walsöe de Reca
Centro de Investigaciones en Sólidos (CINSO), Instituto de Investigaciones Científicas y Técnicas de las Fuerzas Armadas-Consejo Nacional de Investigaciones Científicas y Técnicas (CITEFA-CONICET), J.B. de La Salle 4397, 1603 Villa Martelli, Pcia. de Buenos Aires, Argentina

A. F. Craievich and M. C. A. Fantini
Instituto de Física, Universidade de São Paulo, Rua do Matão Travessa R 187, 05508-900 São Paulo, São Paulo, Brazil

R. J. Prado
Departamento de Física, Instituto de Ciências Exatas e da Terra, Universidade Federal de Mato Grosso, Av. Fernando Corrêa s/n, Coxipó, 78060-900 Cuiabá, Mato Grosso, Brazil

(Received 6 June 2007; accepted 28 February 2008)

Crystal and local structures (long- and short-range order, respectively) of four nanocrystalline zirconia-based solid solutions—ZrO_2-6 and 16 mol % CaO and ZrO_2-2.8 and 12 mol % Y_2O_3—synthesized by a *p*H-controlled nitrate-glycine gel-combustion process were studied. These materials were characterized by synchrotron X-ray diffraction (XRD) and extended X-ray absorption fine structure (EXAFS) spectroscopy. Our XRD results indicate that the solid solution with low CaO and Y_2O_3 contents (6 and 2.8 mol %, respectively) exhibit a tetragonal crystallographic lattice, and those with higher CaO and Y_2O_3 contents (16 and 12 mol %, respectively) have a cubic lattice. Moreover, our EXAFS study demonstrates that the tetragonal-to-cubic phase transitions, for increasing CaO and Y_2O_3 contents, are both related to variations in the local symmetry of the Zr–O first neighbor coordination sphere. © *2008 International Centre for Diffraction Data.* [DOI: 10.1154/1.2903503]

Key words: synchrotron X-ray diffraction, nanocrystalline powders, EXAFS, gel-combustion, zirconia

I. INTRODUCTION

Zirconia-based ceramics have been investigated intensely because of their excellent electric and mechanical properties. In particular, TZP (tetragonal zirconia polycrystals) ceramics exhibit high ionic conductivity at intermediate temperatures and high-fracture toughness (Lee and Rainforth, 1994; Juárez *et al.*, 1999).

These materials have many interesting applications. For example, ZrO_2–CeO_2 substitutional solid solutions are extensively used as redox or oxygen storage promoters in three-way catalysts (Trovarelli, 2002), but ZrO_2–Y_2O_3 ceramics are used for several electrochemical devices (Deportes *et al.*, 1994) and biomedical applications (Yaparpalvi *et al.*, 1994). ZrO_2–CaO is used as an inert matrix for nuclear reactors (Hellwig *et al.*, 2006), as a toughness enhancer for synthetic bone (Silva and Lameiras, 2000), and as a refractory oxide for high-temperature furnaces (Durrani *et al.*, 2006).

Pure zirconia exhibits three stable phases over different temperature ranges with monoclinic, tetragonal, and cubic crystallographic structures (Lee and Rainforth, 1994; Juárez *et al.*, 1999). The cubic phase of all these solid solutions has a fluorite-type structure. The monoclinic phase is stable below 1473 K, the tetragonal phase between 1473 and 2553 K, and above 2553 K the cubic phase is stable up to the melting point (2988 K). The cubic phase can be fully stabilized by cooling down to room temperature solid solutions with other oxides such as Y_2O_3, CaO, MgO, and CeO_2. In contrast, the tetragonal phase of these solid solutions can be retained at room temperature, in a metastable condition, only in nanocrystalline powders or very fine-grained ceramics (Juárez *et al.*, 1999).

The tetragonal phase exhibits three different forms: t, t', and t''. All these forms belong to the $P4_2/nmc$ space group (Yashima *et al.*, 1994, 1996, 1998; Lamas and Walsöe de Reca, 2000; Lamas *et al.*, 2003). The stable tetragonal form is the t-form, which is restricted to the solubility limit predicted by the equilibrium phase diagram. The t'-form has wider solubility but is unstable in comparison with the mixture of t-form and cubic phase. Finally, the t''-form has an axial ratio c/a of unity, but with the oxygen atoms displaced along the c axis from their ideal sites of the cubic phase ($8c$ sites of the $Fm\bar{3}m$ space group).

The local structures around the cations in the tetragonal phase of the metastable forms of nanocrystalline ZrO_2-based solid solutions have not been completely studied yet. Previous studies of these systems deal with nanostructured ZrO_2–CeO_2 solid solutions (Trovarelli, 2002; Vlaic *et al.*, 1997, 1999; Fornasiero *et al.*, 1999; Fábregas *et al.*, 2006) and ZrO_2–Y_2O_3 nanopowders (Yuren *et al.*, 1994; Chadwick *et al.*, 2001), but no investigation regarding ZrO_2–CaO solid solutions have been published yet.

In the present work, the crystalline and local structures of a number of nanocrystalline zirconia-based solid solutions, synthesized by a nitrate-glycine gel-combustion route, were investigated by means of synchrotron XRD and EXAFS spectroscopy. The use of a synchrotron radiation XRD setup made possible the detection of very weak Bragg peaks

corresponding to the tetragonal phase that are forbidden for cubic fluorite-type (FCC) structure. Among all these weak reflections, we have selected for our analysis the strongest one: the (112) reflection.

EXAFS was used to confirm the tetragonal/cubic phase determined by synchrotron radiation XRD and to investigate the variations of the local atomic structure around the metal ions (Zr and Ca or Y). We suggest that the tetragonal/cubic transition observed by synchrotron radiation XRD is only related to a tetragonal-to-cubic change in the Zr–O bond (Fábregas *et al.*, 2006; Fábregas *et al.*, 2008).

II. EXPERIMENTAL

A. Synthesis of nanocrystalline ZrO_2-CaO and $ZrO_2-Y_2O_3$ solid solutions

ZrO_2-6 and 16 mol % CaO and ZrO_2-2.8 and 12 mol % Y_2O_3 nanopowders were synthesized by a *p*H-controlled nitrate-glycine and citric acid, respectively, gel-combustion process (Lamas *et al.*, 2001, 2003, 2005; Lascalea *et al.*, 2004). High-purity (>99.9%) raw compounds were used. For all compositions, the synthesis process was adjusted to obtain 4 g of the final product.

$ZrOCl_2 \cdot 8H_2O$ (99.9%, Alpha Aesar, Ward Hill, Massachusetts) and $CaCO_3$ (Merck, Germany, 99.95%) or Y_2O_3 (99.99%, GFS Chemicals, United Kingdom) were dissolved in 50 ml of nitric acid (65%, Merck, Darmstadt, Germany) in a ratio corresponding to the selected final composition, and this solution was concentrated by thermal evaporation in order to eliminate chloride anions. Glycine (99%, Merck, Darmstadt, Germany) and citric acid (99%, Merck, Darmstadt, Germany) were added in a proportion of 6 and 2.5 moles per mole of metal atom, respectively, and the *p*H of the solution was adjusted in the range of 3 to 7 with ammonium hydroxide (25%, Merck, Darmstadt, Germany). The *p*H was tuned as close as possible to 7, taking care of avoiding precipitation. The resulting solution was concentrated by evaporation using a hot plate at 200 °C until a viscous gel was obtained. This hot gel finally burnt out as a result of a vigorous exothermic reaction. The system remained homogeneous during the whole process and no precipitation was observed. Finally, the as-reacted material was calcined in air at 600 °C for 2 h in order to remove the organic residues.

B. Synchrotron XRD experiments and data analysis

Synchrotron XRD measurements were carried out using the XPD beamline (Ferreira *et al.*, 2006) of the synchrotron radiation facility at the National Synchrotron Light Laboratory (LNLS), Campinas, Brazil. A high-intensity/low-resolution ($\Delta d/d=0.0015$, $2\theta=90°$) configuration, without a crystal analyzer, was employed. This configuration yields four times the signal-to-noise ratio as compared to the high resolution configuration. Because of the inherent very broad Bragg peaks corresponding to nanocrystalline materials, the rather low resolution of the experimental setup does not significantly affect the values of the structural parameters derived from our XRD measurements. The wavelength was set at 1.549 84 Å. Diffraction data within the angular 2θ range 20° to 130° were collected at room temperature in step-scanning mode, with a step of 0.05°, and a counting time of 3 s/step.

The average crystallite size of the nanocrystalline powders was estimated from the width of the XRD peaks using the Scherrer equation considering the instrumental broadening (Klug and Alexander, 1974). The average size ranges from 7 to 15 nm for the different studied compositions.

1. Direct determination of the oxygen-ion displacement

The reflections with mixed, odd, and even, Miller indexes are forbidden for structures with a cubic FCC lattice, such as fluorite-type structures, but among them those with l even and h and k odd are allowed for structures with tetragonal lattice. These reflections are related only to displacements of oxygen anions from their positions on the cubic lattice along the c axis. For the (112) reflection, the structure factor including the Debye-Waller effect of temperature is given by (Giacovazzo, 1992)

$$|F(112)|^2 = 64 f_O^2 q_O^2 \sin^2[4\pi z(O)], \tag{1}$$

where f_O^2 is the atomic scattering factor of O^{2-}, q_O^2 is its temperature factor, and $z(O)$ is the fractional z coordinate of the O^{2-} anion in the asymmetric unit of the tetragonal unit cell. Differently, the structure factor associated to the (111) Bragg reflection only depends on the cationic sublattice, as shown by the corresponding modulus of the structure factor

$$|F(111)|^2 = 16 f_{Zr-A}^2 q_{Zr-A}^2, \tag{2}$$

where A is either Y^{3+} or Ca^{2+}, f_{Zr-A}^2 is the average atomic scattering factor of Zr^{4+}, and A cations and q_{Zr-A}^2 is their average temperature factor.

Therefore, the displacement of the oxygen anions from their positions in the cubic phase can be calculated from the ratio of the intensities of the (112) and (111) peaks. The integrated intensities of powder diffraction Bragg peaks are given by

$$I_{hkl}(2\theta) = K|F(hkl)|^2 m(hkl) L(\theta) P(\theta), \tag{3}$$

where $F(hkl)$ is the structure factor given by Eqs. (1) or (2), $m(hkl)$ is the multiplicity factor, $L(\theta)$ is the Lorentz factor, $P(\theta)$ is the polarization factor, and K is a constant. For powder diffraction and symmetrical θ-2θ scan, $L(\theta) = \cos(\theta)/\sin^2(\theta)$. For X-rays coming from a synchrotron source using a horizontal diffraction axis, $P \cong 1$. Since $m(111)=m(112)=8$, the $I(112)/I(111)$ quotient results in

$$\frac{I(112)}{I(111)} = \frac{4 f_O^2 \sin^2[4\pi z(O)] q_O^2 L_{112}}{f_{Zr-A}^2 q_{Zr-A}^2 L_{111}}. \tag{4}$$

Thus, neglecting the effect of the temperature factors, the fractional z coordinate of the oxygen atom in the asymmetric unit, $z(O)$, can easily be determined from the measured integrated intensities, $I(112)$ and $I(111)$, using Eq. (4).

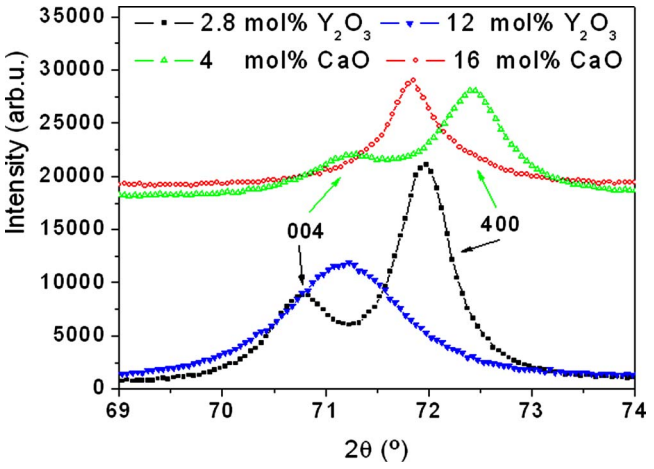

Figure 1. (Color online) Synchrotron XRD data close to the (004) and (400) peaks.

2. Rietveld analysis

In order to determine the parameters of the unit cell and the z(O) coordinate as a function of the dopant content, Rietveld refinements of the XRD data were performed using the FULLPROF program (Rodríguez-Carvajal, 1990). For the tetragonal phase, the $P4_2/nmc$ space group was assumed, with (Zr^{4+}, Ca^{+2}, or Y^{3+}) cations and O^{2-} anions in 2a and 4d positions, respectively. The results of these refinements were given in terms of the usual pseudo-fluorite unit cell (Lee and Rainforth, 1994). For the cubic phase (with a fluorite-type structure), the $Fm\bar{3}m$ space group was applied, with (Zr^{4+}, Ca^{+2}, or Y^{3+}) cations and O^{2-} anions in 4a and 8c positions, respectively.

The peak shape was assumed to be well described by a pseudo-Voigt function. The background of each profile was adjusted by a six-parameter polynomial function in $(2\theta)^n$, $n=0$ to 5. Isotropic atomic temperature parameters were used. The thermal parameters corresponding to Zr and Ca or Y atoms were assumed to be equal.

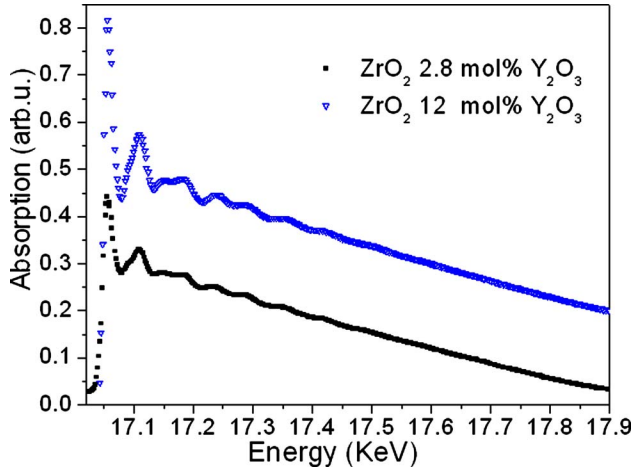

Figure 2. (Color online) X-ray absorption spectra at the Y K-edge.

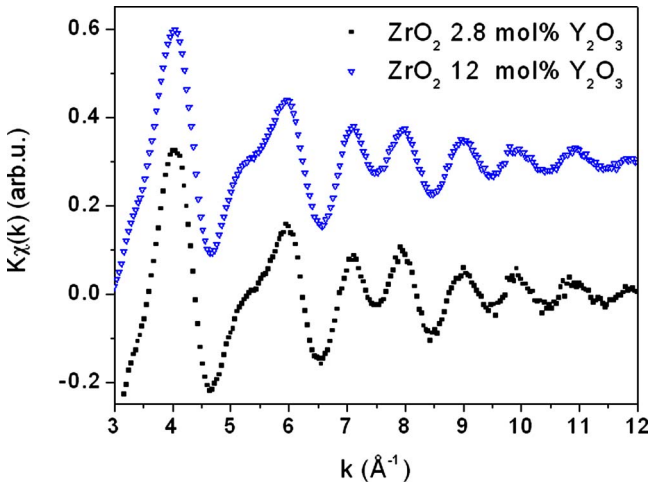

Figure 3. (Color online) k-weighted raw EXAFS data at the Y K-edge.

C. X-ray absorption spectroscopy and data analysis

EXAFS spectra were measured at the D04B-XAFS1 beamline (Tolentino *et al.*, 1998) (LNLS) in transmission mode using a Si (220) monochromator for the Zr and Y K-edges, but it was not possible to get good data for the Ca K-edge. The nominal photon flux of the beamline is 3×10^9 photons/(s·mrad·100 mA)@6 keV. The energy range was 17900 to 18900 eV for Zr K-edge and 16 900 to 17 900 eV for Y K-edge and was calibrated using a Zr foil. Data were collected at room temperature using energy steps of 2 eV and $E/\Delta E=5000$ to 10 000. The integration time was 4 s for the Zr K-edge and 6 s for the Y K-edge. Two spectra were collected for each sample and the average spectrum was used to perform the data analysis. The samples were prepared by deposition from a powder suspension in isopropanol on a Millipore membrane. The thickness was adjusted to obtain a total absorption above the edge of 1.5. Since the photon flux at the D04B-XAFS1 beamline is not enough to get quality data at the Ca K-edge, it was not possible to study it.

To obtain the So value for the Zr K-edge required for coordination number determination, the standard compound $BaZrO_3$ (6 oxygen atoms at 2.099 Å) was used, obtaining a value of 0.9.

EXAFS data reduction was performed using the WINXAS program (Ressler, 1998). Both pre- and post-edge free-atom contributions were subtracted from raw data. For the pre-edge region, a linear fit of the absorption signal was subtracted from the experimental data; a fifth-order polynomial was used for the post-edge removal.

In order to study the local structure around Zr, selected Fourier transform (FT) windows were 3 to 12 Å^{-1} and 1 to 4 Å in k- and R-space, respectively. A k^3-weighted os-

TABLE I. Average crystallite size of all the nanocrystalline ZrO_2 based powders, as determined by the Scherrer equation.

CaO content (mol%)	D (nm)	Y_2O_3 content (mol%)	D (nm)
4	13.6(5)	2.8	15 (1)
16	14.5(5)	12	7.3 (5)

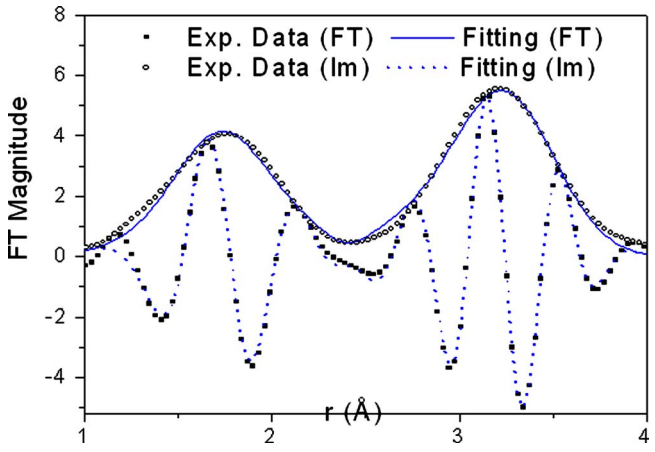

Figure 4. (Color online) Fourier transforms of the EXAFS functions corresponding to ZrO_2-12 mol% Y_2O_3 solid solutions at the Zr *K*-edge and corresponding fit.

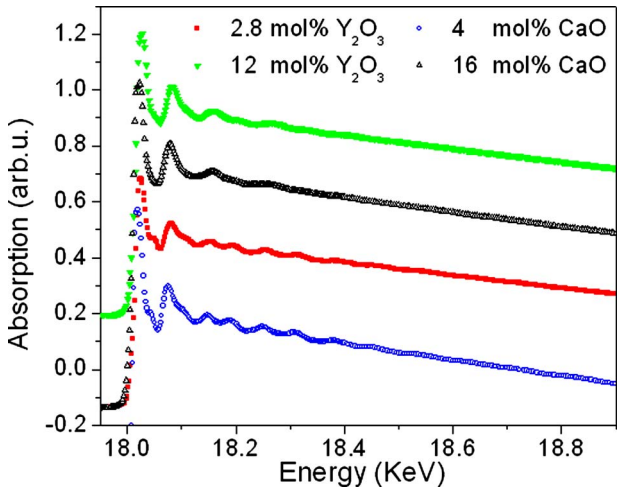

Figure 5. (Color online) X-ray absorption spectra at the Zr *K*-edge.

cillation was used to calculate the Fourier transform. The quantitative fitting was performed with a k^3-weighted oscillation using the FEFFIT program (Ankudinov *et al.*, 1998) with theoretical amplitudes and phases calculated with the FEFF8 program (Newville *et al.*, 1995).

1. Model 1

The free parameters used in this model for the fitting procedure for the Zr first sphere (Zr-oxygen bond) were two coordination numbers (CNs), two bond lengths (DIST), and one common Debye-Waller (DW) parameter (σ). According to Vlaic *et al.* (1999) and Fornasiero *et al.* (1999), the values of E_O and σ were considered to be equivalent for both Zr-O subshells. The second sphere (cation-cation bond), for tetragonal samples, was modeled using two cation-cation distances with the CNs fixed according to the nominal composition (with a common DW parameter). Only one cation-cation distance with CN fixed according to nominal composition, but with different DW values whether it was Zr-Ca, or Zr-Y or Zr-Zr, was used for the cubic samples. All the distances were correlated using a crystallographic model based on the cell parameters, *a* and *c*, and the fractional *z* coordinate of the O^{2-} anion in the asymmetric unit of the tetragonal unit cell, *z*(O). The inner potential shift (ΔE_O) was considered to be equal for all the subshells.

Since Zr and Y are neighbors in the periodic table, they are essentially not distinguished in XRD or EXAFS measurements. Consequently, the second sphere (cation-cation bond) was modeled using two cation-cation distances with the CNs fixed at 4 and 8 (with a common DW parameter) for the tetragonal samples, and one cation-cation distance with the CN fixed at 12 for the cubic ones, for the EXAFS signals close to both cation edges. The inner potential shift was considered to be equal for all subshells.

2. Model 2

For this model, we fixed the coordination around Zr in a 4+4 shell, but in this case each subshell has different σ parameters but equal E_O. For cubic samples, a fixed CN of 7 was used. The second subshell was treated as in Model 1. Both theoretical studies on ZrO_2–Y_2O_3 (Stapper *et al.*, 1999; Fabris *et al.*, 2002) and X-ray and neutron diffraction experiments on cubic monocrystals (Horiuchi *et al.*, 1984; Morinaga *et al.*, 1980; Steele, 1996) have shown that oxygen atoms can be displaced from their ideal sites in non-

TABLE II. Structural parameters and standard Rietveld agreement factors obtained for the nanocrystalline ZrO_2-Y_2O_3 powders calcined at 600 °C. The values of *z*(O) determined from *I*(112) and *I*(111) are also reported.

	2.8 mol% Y_2O_3 $P4_2/nmc$	12 mol% Y_2O_3 $Fm\bar{3}m$	6 mol% CaO $P4_2/nmc$	16 mol% CaO $Fm\bar{3}m$
c (Å)	5.1762(3)	5.14729(7)	5.1609 (8)	5.102 (2)
a (Å)	5.1015(3)		5.1025 (7)	
c/*a*	1.0146(1)		1.0114 (3)	
z(O) Rietveld	0.207(1)	0.250	0.2101 (8)	0.25
z(O) *I*112/*I*111	0.212(1)	0.250	0.219 (1)	0.25
B(Zr;*A*) (Å^2)	0.75(2)	0.99(2)	0.89 (2)	1.26 (4)
B(O) (Å^2)	1.97(7)	2.89(7)	1.81 (8)	3.3 (1)
R_p	3.02	6.17	4.2	5.53
R_{wp}	4.63	7.74	3.31	3.84
R_{exp}	0.920	1.27	1.08	1.06

TABLE III. Results of the EXAFS analysis at the Y *K*-edge for all the studied nanostructured ZrO_2-Y_2O_3 solid solutions; CN is coordination number, "Dist." is Zr-oxygen distance, σ^2 is Debye-Waller parameter, ΔE_o is inner potential shift, and *R* is goodness-of-fit.

Y_2O_3 content (mol%)	First Sphere			Second Sphere			ΔE_o	
	CN	Dist. (Å)	σ^2 (Å^2)	CN	Dist. (Å)	σ^2 (Å^2)	(eV)	*R* (%)
2.8	7.9(8)	2.31(1)	0.0090(1)	4 8	3.64(3) 3.64(3)	0.0082(7)	3.7	0.7
12	7.5(8)	2.32(1)	0.0105(8)	12	3.61(3)	0.0116(9)	1.4	1.8

crystallographic directions. As a result, the distribution of Zr-O distances is very wide and non-Gaussian. Thus, the use of a DW parameter alone is not enough to describe these bonds for $ZrO_2-Y_2O_3$. Consequently, for samples with high Y_2O_3 content, we have used the same parameters as in Model 1, but in this case we have included the third cumulant expansion for the oxygen in the first sphere for the Zr *K*-edge.

III. RESULTS AND DISCUSSION

A. XRD analysis

A qualitative analysis of the XRD patterns indicates that the crystallographic structures of the samples with low CaO and Y_2O_3 content (ZrO_2-6 mol% CaO and ZrO_2-2.8 mol% Y_2O_3) are tetragonal, but those corresponding to high CaO and Y_2O_3 contents (ZrO_2-16 mol% CaO and ZrO_2-12 mol% Y_2O_3) are cubic.

The average crystallite size of all studied nanocrystalline powders estimated from the width of the XRD peaks using the Scherrer equation (Klug and Alexander, 1974) are reported in Table I. Errors in crystallite size were determined by estimating the error in the full width at half-maximum to be equal to the 2θ step. Strain analysis was not carried out.

Figure 1 displays the peak profiles of the (400) and (004) Bragg reflections corresponding to all the studied samples. Only one diffraction peak is observed for ZrO_2-16 mol% CaO and ZrO_2-12 mol% Y_2O_3 powders, thus indicating the presence of a cubic phase. On the contrary, the XRD patterns of the ZrO_2-6 mol% CaO and ZrO_2-2.8 mol% Y_2O_3 solid solutions exhibit a splitting of the (400) and (004) peaks. This indicates the presence for these solutions of a tetragonal phase with $c/a > 1$.

The conclusions specified above, based on the visual examination of only two Bragg peaks of XRD data, were corroborated by a Rietveld fitting, which makes a global analysis of the whole XRD pattern. The parameters derived from Rietveld refinements are summarized in Table II.

Table II reports the oxygen ion displacement as a function of CaO and Y_2O_3 contents determined from Rietveld refinements and also from the analysis of the ratio of the (112) and (111) integrated intensities. The differences between the displacements obtained by both methods are because the whole XRD pattern is fitted in the Rietveld method—the weight of the very weak peaks such as the (112) being very low.

B. EXAFS analysis

1. Y *K-edge*

The X-ray absorption spectra and the EXAFS signals corresponding to the Y *K*-edge of ZrO_2-2.8 and 12 mol% Y_2O_3 samples are displayed in Figures 2 and 3, respectively. A good signal/noise ratio is observed for both spectra up to 12 Å^{-1}. A visual examination of the results plotted in Figure 3 indicate that the EXAFS signals corresponding to both samples (with 2.8 mol% and 12 mol% Y_2O_3) are very similar, thus indicating that the local structure around the Y at-

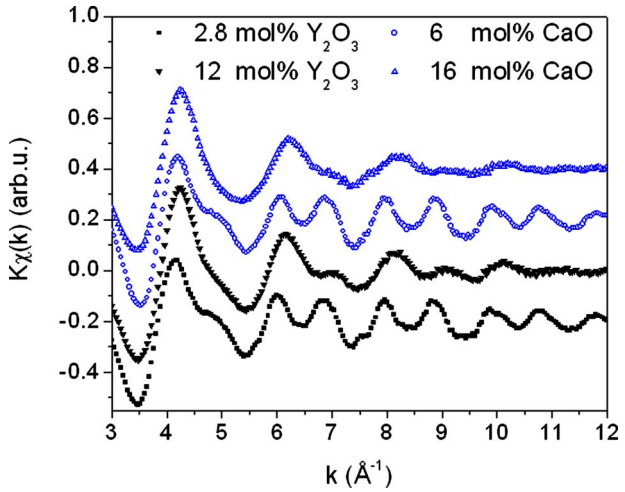

Figure 6. (Color online) *k*-weighted raw EXAFS data at the Zr *K*-edge.

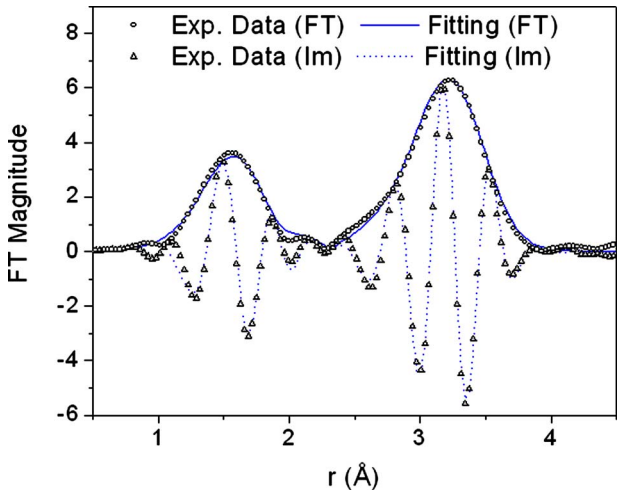

Figure 7. (Color online) Fourier transforms of the EXAFS functions corresponding to ZrO_2-6 mol% CaO solid solutions at the Zr *K*-edge and corresponding fit.

TABLE IV. Results of the EXAFS analysis for all the studied nanostructured ZrO_2 based solid solutions for Model 1; CN is coordination number, "Dist." is Zr-oxygen distance, σ^2 is Debye-Waller parameter, "3rd cumul." is third cumulant, ΔE_o is inner potential shift, and R is goodness-of-fit.

	First Sphere			Second Sphere						
CaO content (mol%)	CN	Dist. (Å)	σ^2 (Å^2)	CN Zr	CN Ca	Dist. (Å)	σ^2 (Å^2) Zr-Zr	σ^2 (Å^2) Zr-Ca	ΔE_o (eV)	R (%)
6	4.1(4)	2.11(1)	0.0055(4)	3.8	0.24	3.60(3)	0.010(1)	0.0022(2)	−1.6	2.12
	2.0(2)	2.32(1)		7.5	0.48	3.62(3)				
16	6.1(6)	2.14(1)	0.0085(7)	10.1	—	3.62(3)	0.019(2)	0.0045(4)	−1.5	2.45
				—	1.9	3.62(3)				

	First Sphere			Second Sphere					
Y_2O_3 content (mol%)	CN	Dist. (Å)	σ^2 (Å^2)	3rd cumul.	CN	Dist. (Å)	σ^2 (Å^2)	ΔE_o (eV)	R (%)
2.8	4.2(4)	2.09(1)	0.0073(6)	0.000 33	4	3.63(3)	0.009(9)	1.6	1.1
	2.3(2)	2.36(1)		0.004 07	8	3.63(3)			
12	6.4(6)	2.19(1)	0.0077(6)	0.000 88	12	3.57(3)	0.016(1)	3.5	1.9

oms is essentially the same. Also important is that the shape and amplitude are different from that of the Zr K-edge.

The FT of the EXAFS spectra near the Y K-edge (without phase correction) corresponding to the 12 mol% Y_2O_3 sample are displayed in Figure 4. The first peak is associated to the oxygen nearest neighbors of Y atoms, and the second peak is associated to the first neighbor's cation shell. In the same figure a fitted curve is plotted as an example of the good agreement obtained between the EXAFS signal derived from the proposed model and experimental data.

The Y-O bond is modeled using a single oxygen first shell (without subshells) for which the CNs are approximately equal to 8. Table III reports the results of the fitting procedure assuming one oxygen shell with a variable CN. For both samples, the CN is undistinguishable from 8, within the error bars. The Y-O distance and DW parameters are very similar, within the error bars, and the first neighbor distance coincides with those reported by Li *et al.* (1993). As in the case of Zr K-edge, the difference between the values of E_O for different samples was not larger than two energy steps (4 eV).

The results obtained from the EXAFS analysis of the second shell around Y are summarized in Table III. We notice that the cation-cation distances exhibit a slight decreasing trend for increasing Y_2O_3 content. The Debye-Waller parameter also increases with increasing Y_2O_3 content.

2. Zr K edge

The X-ray absorption spectra and EXAFS signals corresponding to the Zr K-edge are plotted in Figures 5 and 6, respectively. A good signal/noise ratio can be noticed up to 12 Å^{-1}. In Figure 6, the shoulder observed near 6.8 and 8.8 Å^{-1} in the EXAFS signal corresponding to ZrO_2-2.8 mol% CaO and ZrO_2-6 mol% Y_2O_3 is not apparent in the signal of ZrO_2-12 mol% CaO and ZrO_2-16 mol% Y_2O_3, clearly indicating that a structural change occurs.

The FT of the EXAFS function (without phase correction) corresponding to 6 mol% CaO sample, at the Zr K-edge, is shown in Figure 7. The FT exhibits two main peaks, the first corresponding to the Zr-O nearest neighbor shell and the second associated to the Zr-cation (Zr-Zr and

TABLE V. Results of the EXAFS analysis for all the studied nanostructured ZrO_2-based solid solutions for Model 2; CN is coordination number, "Dist." is Zr-oxygen distance, σ^2 is Debye-Waller parameter, "3rd cumul." is third cumulant, ΔE_o is inner potential shift, and R is goodness-of-fit.

	First Sphere			Second Sphere						
CaO content (mol%)	CN	Dist. (Å)	σ^2 (Å^2)	CN Zr	CN Ca	Dist. (Å)	σ^2 (Å^2) Zr-Zr	σ^2 (Å^2) Zr-Ca	ΔE_o (eV)	R (%)
6	4	2.11(1)	0.0055(4)	3.8	0.24	3.61(3)	0.010(1)	0.0014(1)	−1.3	3.0
	4	2.32(1)	0.017(1)	7.5	0.48	3.61(3)				
16	7	2.14(1)	0.0098(8)	10.1	—	3.61(3)	0.019(2)	0.0041(4)	−2.0	3.0
				—	1.9	3.61(3)				

	First Sphere			Second Sphere					
Y_2O_3 content (mol%)	CN	Dist. (Å)	σ^2 (Å^2)	3rd cumul.	CN	Dist. (Å)	σ^2 (Å^2)	ΔE_o (eV)	R (%)
2.8	4	2.34(1)	0.0062(6)	—	4	3.61(3)	0.0094(8)	1.1	2.0
	4	2.11(1)	0.018(1)	—	8	3.63(3)			
12	7	2.19(1)	0.0077(6)	0.00088	12	3.58(3)	0.016(1)	3.5	1.6

TABLE VI. Average cation-oxygen (Cat-O) distances determined from the results of EXAFS analysis for the Zr–O bond in ZrO_2-CaO solid solutions (assuming a Ca–O distance of 2.45 Å) compared to synchrotron radiation XRD data.

	Average EXAFS data (Model 1)		Average EXAFS data (Model 2)		Synchrotron radiation XRD data	
CaO content (mol%)	*d*(Cat-O1) (Å)	*d*(Cat-O2) (Å)	*d*(Cat-O1) (Å)	*d*(Cat-O2) (Å)	*d*(Cat-O1) (Å)	*d*(Cat-O2) (Å)
4	2.12(2)	2.33(2)	2.11(2)	2.34(2)	2.119(5)	2.330(5)
16	2.19(2)		2.20(2)		2.2091(9)	

Zr-Y or Ca) and second Zr-O coordination shells. In the same figure, one of the results of the fitting procedure is plotted as an example of the good agreement obtained between the proposed model and EXAFS data. Similar results were obtained for all the other compositions.

In the present work, EXAFS analysis at the Zr *K*-edge was performed using the two models that were described in a preceding section. We have concluded that both of them lead to statistically identical fittings with similar quality.

Tables IV and V summarize the results of the EXAFS analysis for Models 1 and 2, respectively. It can be noticed that for low CaO or Y_2O_3 content two different Zr-O distances ($d_{Zr–O1}$ and $d_{Zr–O2}$) are apparent (the two distances from Zr for the different subshells will hereafter be named Zr-O1 and Zr-O2).

For samples with high dopant concentration, i.e., 16 mol% CaO and 12 mol% Y_2O_3, the results of EXAFS analysis exhibit clear differences as compared to those of lower dopant content. For high CaO or Y_2O_3 contents, we observed only one Zr-O distance for both models. Thus, the tetragonal-to-cubic transition observed by synchrotron radiation XRD for increasing dopant content appears to be only related to a tetragonal-to-cubic change in symmetry of the Zr-O bond for ZrO_2-Y_2O_3 solid solutions and very probably also for ZrO_2-CaO materials. The same finding was previously reported in a similar study of the ZrO_2-CeO_2 system (Fábregas *et al.*, 2006).

Model 1 gives the nearest neighbor distances that are equal, within the error bars, to those reported by Li *et al.* (1993) and Rush *et al.* (2000) for the 12 mol% Y_2O_3 cubic sample. For Model 2, the third cumulant expansion was necessary for the cubic ZrO_2-Y_2O_3 sample. The rather high Y_2O_3 content introduces significant static disorder (Stapper *et al.*, 1999; Fabris *et al.*, 2002; Steele, 1996), so in this case the bonds cannot be adequately described by a simple Gaussian distribution.

We can notice, for Model 1, that the average CN for the second subshell in the tetragonal samples and the total coordination number in the cubic subshell are rather low. In these samples, these low coordinations can be explained as a consequence of the large amount of oxygen vacancies that the dopant introduces into the system. This argument is less valid for the tetragonal samples, because the oxygen vacancy concentration is expected to be lower. On the other hand, it is well known that the strong covalent nature of Zr-O bonding in ZrO_2 lattice promotes sevenfold coordination (Ho, 1982), as observed in monoclinic ZrO_2. Therefore, we can expect that the Zr atoms also exhibit this type of coordination in the tetragonal phase.

Considering the CN and Debye-Waller parameters obtained for Models 1 and 2, we believe that the local order in zirconia-based materials is more complex than our analysis suggests. From crystallographic arguments, we know that both oxygen subshells are equivalent, so they should have the same Debye-Waller factor and coordination. In this respect, we could not find a structural model for fitting of the EXAFS data that accomplishes this requisite and at the same time leads to the nearest neighbor distances compatible with those obtained from XRD data. Therefore, we cannot distinguish between both models in order to determine the local order.

Our EXAFS measurements probed the average local structures around Zr atoms. On the other hand, for a substitutional solid solution such as those studied here, the crystal structure determined by XRD corresponds to the average of local structures over all unit cells. The averaging over the unit cells leads to two different average cation-oxygen distances, $d(\text{cation}–\text{O}_i)$ $(i=1,2)$. Considering also the oxygen vacancies, we used [as explained in Fábregas *et al.* (2006)]

$$d(\text{cation}-\text{O}i) = \frac{d(\text{Zr}-\text{O}i)(1-X)(\text{CN}_{\text{Zr}}/8) + d(A-\text{O})X(\text{CN}_A/8)}{(1-X)(\text{CN}_{\text{Zr}}/8) + X(\text{CN}_A/8)} \quad (i=1,2), \tag{5}$$

where CN_{Zr} and CN_A are the total coordinations around Zr and dopant cations, respectively, determined from EXAFS analysis (the total coordination of Ca was assumed to be 8), X is the molar fraction of dopant atoms, and $d(\text{Zr}–\text{O1})$, $d(\text{Zr}–\text{O2})$, and $d(A–\text{O})$ are the distances of the Zr-O1, Zr-O2, or dopant-O bonds (the Ca-O distance was as-

TABLE VII. Average cation-oxygen distances determined from the results of EXAFS analysis for the Zr–O and Y–O bonds in ZrO_2-Y_2O_3 solid solutions compared to synchrotron radiation XRD data.

	Average EXAFS data (Model 1)		Average EXAFS data (Model 2)		Synchrotron radiation XRD data	
CaO (mol%)	*d*(Cat-O1) (Å)	*d*(Cat-O2) (Å)	*d*(Cat-O1) (Å)	*d*(Cat-O2) (Å)	*d*(Cat-O1) (Å)	*d*(Cat-O2) (Å)
2.8	2.11(2)	2.36(2)	2.12(2)	2.34(2)	2.111(5)	2.340(5)
12	2.22(2)		2.22(2)		2.228 84(5)	

sumed to be 2.45 Å). The values for the Ca-O bond were selected based on first, CN of the dopant atom is always found to be near 8 at a practically constant distance (Vlaic *et al.*, 1997, 1999; Fornasiero *et al.*, 1999; Fábregas *et al.*, 2006, 2008; Li *et al.*, 1993; Mastelaro *et al.*, 2003; Ho, 1982; Rush *et al.*, 20003), and second, the eightfold coordination is the expected one by crystallography. The 2.45 Å constant value was chosen after a bibliographical search of Ca-O distances determined directly from measurements on the Ca *K*-edge or from compounds with a known and well-defined environment around Ca (Khan *et al.*, 1998; Sowrey *et al.*, 2004; Pattanaik *et al.*, 2004; Tommaseo and Kersten, 2002; Peters *et al.*, 2000).

As reported in Table VI (for ZrO_2-CaO), Table VII (for ZrO_2-Y_2O_3), and Figure 8, the *d*(cation–O1) and *d*(cation–O2) distances obtained from the EXAFS results using Eq. (5) agree very well, for both models, with those determined independently from synchrotron radiation XRD data using the simple expressions

$$d(\text{cation}-\text{O1}) = [0.125 \times a^2 + (z(\text{O}) \times c)^2]^{1/2}, \quad (6a)$$

$$d(\text{cation}-\text{O2}) = [0.125 \times a^2 + (0.5 - z(\text{O}))^2 \times c^2]^{1/2}, \quad (6b)$$

where a and c are the unit cell parameters and z(O) is the fractional z coordinate of the oxygen atom in the asymmetric unit.

The increase in the DW parameters for cubic samples is probably related to distortions in Zr polyhedra (Li *et al.*, 1993) produced by the addition of a rather high amount of Ca atoms in the solid solutions.

Tables IV and V also report the structure parameters obtained from EXAFS analysis of the second shell around Zr. The cation-cation distances exhibit a slight decreasing trend for increasing dopant content. On the other hand, the Debye-Waller parameter increases with increasing dopant content. This effect could be related to the severe distortion of Zr polyhedra (Li *et al.*, 1993) generated by the introduction of dopants in the system lattice. Thus, it is to be expected that the DW parameter increases for cubic samples, with rather high dopant content. Finally, we notice that the cation-cation distances decrease slightly with increasing dopant content—this being consistent with unit cell parameters shrinking when passing from the tetragonal to the cubic structure.

IV. CONCLUSION

We have clearly identified by synchrotron XRD the presence of a tetragonal phase and a cubic phase in ZrO_2-CaO and ZrO_2-Y_2O_3 solid solutions prepared by gel-combustion processes. EXAFS analysis demonstrated that the tetragonal-to-cubic compositional transitions, for increasing CaO and Y_2O_3 content, are related to a similar symmetry change of the oxygen first shell around Zr cations, which passes from a two-subshell configuration in the tetragonal phase towards a single-shell configuration in the cubic phase.

The present investigation evidenced an excellent agreement of the first neighbor distances revealed by EXAFS and the average cation-oxygen distances determined from synchrotron XRD data, for all the studied solid solutions. This

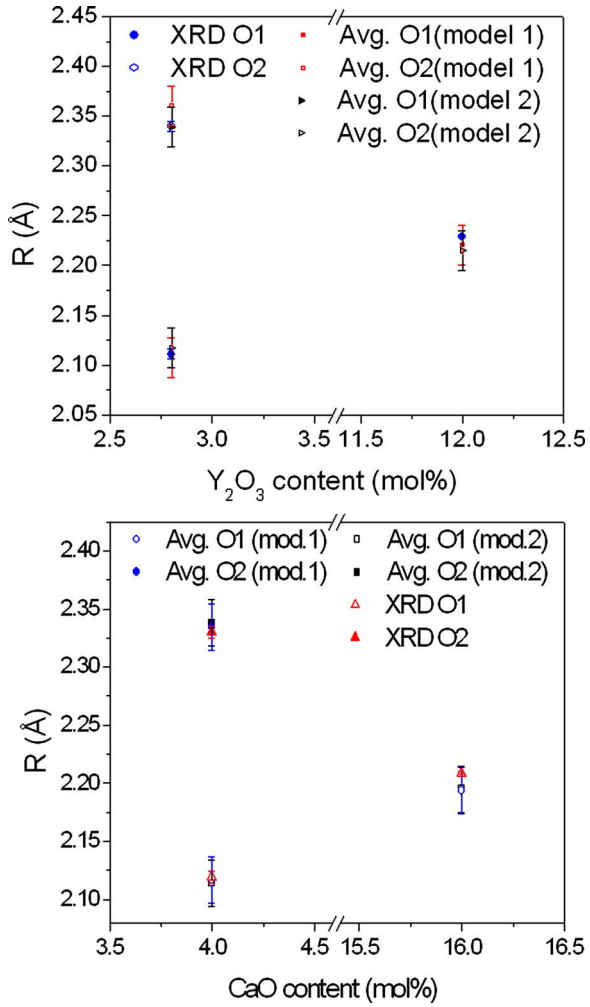

Figure 8. (Color online) Comparison between the average cation-O1 and cation-O2 distances determined from the results of EXAFS analysis and those obtained by synchrotron radiation XRD for zirconia based solutions.

good agreement demonstrates the robustness of the structure model that we have proposed in order to fit EXAFS data.

ACKNOWLEDGMENTS

The present work was performed within the frame of scientific collaboration agreements CAPES-SECyT and CNPq-CONICET between Brazil and Argentina. It was also supported partially by LNLS (Proposals D12A-XRD1-1857, D10B-XPD-2230, D10B-XPD-24276, D04B-XAFS1-2258, and D04B-XAFS1-4204), CNPq (Brazil, PROSUL program), [*Agencia Nacional de Promoción Científica y Tecnológica*] (Argentina, PICT Nos. 14268 and 38309), CONICET (Argentina, PIP No. 6559), and [*Fundación YPF*] (Argentina, Repsol YPF Award 2003).

Ankudinov, A. L., Ravel, B., Rehr, J. J., and Conradson, S. D. (**1998**). "Real-space multiple-scattering calculation and interpretation of x-ray-absorption near-edge structure," Phys. Rev. B **58**, 7565–7576.

Chadwick, A. V., Mountjoy, G., Nield, V. M., Poplett, I. J. F., Smith, M. E., Strange, J. H., and Tucker, M. G. (**2001**). "Solid-state NMR and X-ray studies of the structural evolution of nanocrystalline zirconia," Chem. Mater. **13**, 1219–1229.

Deportes, C., Duclot, M., Fabry, P., Fouletier, J., Hammou, A., Kleitz, M., Siebert, E., and Souquet, J. L. (**1994**). *Electrochimie des Solides* (Presses Universitaires de Grenoble, Grenoble, France).

Durrani, S. K., Akhtar, M., Ahmad, M., and Hussain, M. A. (**2006**). "Synthesis and characterization of low density calcia stabilized zirconia ceramic for high temperature furnace application," Mater. Chem. Phys. **100**, 324–328.

Fábregas, I. O., Fuentes, R. O., Lamas, D. G., Fernández de Rapp, M. E., Walsöe de Reca, N. E., Fantini, M. C. A., Craievich, A. F., Prado, R. J., Millen, R. P., and Temperini, M. L. A. (**2006**). "Local structure of the metal-oxygen bond in compositionally homogeneous, nanocrystalline zirconia-ceria solid solutions synthesized by a gel-combustion process," J. Phys.: Condens. Matter **18**, 7863–7881.

Fábregas, I. O., Lamas, D. G., Acuña, L. M., Fantini, M. C. A., Craievich, A. F., and Prado, R. J. (**2008**). "Crystal structure and local atomic order of nanocrystalline ZrO_2–Y_2O_3 solid solutions II: Extended X-ray absorption fine structure spectroscopy study," J. Phys.: Condens. Matter (in preparation).

Fabris, S., Paxton, A. T., and Finnis, M. W. (**2002**). "A stabilization mechanism of zirconia based on oxygen vacancies only," Acta Mater. **50**, 5171–5178.

Ferreira, F. F., Granado, E., Carvalho, Jr., W., Kycia, S. W., Bruno, D., and Droppa Jr., R. (**2006**). "X-ray powder diffraction beamline at D10B of LNLS: application to the Ba_2FeReO_6 double perovskite," J. Synchrotron Radiat. **13**, 46–53.

Fornasiero, P., Fonda, E., Monte, R. D., Vlaic, G., Kašpar, J., and Graziani, M. (**1999**). "Relationships between structural/textural properties and redox behavior in $Ce_{0.6}Zr_{0.4}O_2$ mixed oxides," J. Catal. **187**, 177–185.

Giacovazzo, C., (Ed.) (**1992**). *Fundamentals of Crystallography (International Union of Crystallography Texts on Crystallography 2)* (Oxford U. P., New York), p. 148.

Hellwig, Ch., Streit, M., Blair, P., Tverberg, T., Klaassen, F. C., Schram, R. P. C., Vettraino, F., and Yamashita, T. (**2006**). "Inert matrix fuel behaviour in test irradiations," J. Nucl. Mater. **352**, 291–299.

Ho, S.-M. (**1982**). "On the structural chemistry of zirconium oxide," Mater. Sci. Eng. **54**, 23–29.

Horiuchi, H., Schultz, A. J., Leung, P. C. W., and Williams, J. M. (**1984**). "Time-of-flight neutron diffraction study of a single crystal of yttria-stabilized zirconia, $Zr(Y)O_{1.862}$, at high temperature and in an applied electric field," Acta Crystallogr., Sect. B: Struct. Sci. **40**, 367–372.

Juárez, R. E., Lamas, D. G., Lascalea, G. E., and Walsöe de Reca, N. E. (**1999**). "Synthesis and structural properties of zirconia-based nanocrystalline powders and fine-grained ceramics," Defect Diffus. Forum **177–178**, 1–26.

Khan, M. S., Islam, M. S., and Bates, D. R. (**1998**). "Cation doping and oxygen diffusion in zirconia: a combined atomistic simulation and molecular dynamics study," J. Mater. Chem. **8**, 2299–2307.

Klug, H. P. and Alexander, L. E. (**1974**). *X-ray Diffraction Procedures for Polycrystalline and Amorphous Materials* (Wiley, New York), 2nd ed., p. 618.

Lamas, D. G., Fuentes, R. O., Fábregas, I. O., Fernández de Rapp, M. E., Lascalea, G. E., Casanova, J. R., Walsöe de Reca, N. E., and Craievich, A. F. (**2005**). "Synchrotron X-ray diffraction study of the tetragonal-cubic phase boundary of nanocrystalline ZrO_2–CeO_2 synthesized by a gel-combustion process," J. Appl. Crystallogr. **38**, 867–873.

Lamas, D. G., Juárez, R. E., Lascalea, G. E., and Walsöe De Reca, N. E. (**2001**). "Synthesis of compositionally homogeneous, nanocrystalline ZrO_2-35 mol% CeO_2 powders by gel-combustion," J. Mater. Sci. Lett. **20**, 1447–1449.

Lamas, D. G., Lascalea, G. E., Juárez, R. E., Djurado, E., Pérez, L., and Walsöe de Reca, N. E. (**2003**). "Metastable forms of the tetragonal phase in compositionally homogeneous, nanocrystalline zirconia-ceria powders synthesised by gel-combustion," J. Mater. Chem. **13**, 904–910.

Lamas, D. G. and Walsöe de Reca, N. E. (**2000**). "X-ray diffraction study of compositionally homogeneous, nanocrystalline yttria-doped zirconia powders," J. Mater. Sci. **35**, 5563–5567.

Lascalea, G. E., Lamas, D. G., Pérez, L., Cabanillas, E. D., and Walsöe de Reca, N. E. (**2004**). "Synthesis of ZrO_2-15 mol% CeO_2 nanopowders by a pH-controlled nitrate-glycine process," Mater. Lett. **58**, 2456–2460.

Lee, W. E. and Rainforth, W. M. (**1994**). *Ceramic Microstructures: Property Control by Processing* (Chapman and Hall, London), p. 317.

Li, P., Chen, I.-W., and Penner-Hahn, J. E. (**1993**). "X-ray-absorption studies of zirconia polymorphs. II. Effect of Y_2O_3 dopant on ZrO_2 structure," Phys. Rev. B **48**, 10074–10081.

Mastelaro, V. R., Briois, V., de Souza, D. P. F., and Silva, C. L. (**2003**). "Structural studies of a ZrO_2–CeO_2 doped system," J. Eur. Ceram. Soc. **23**, 273–282.

Morinaga, M., Cohen, J. B., and Faber, Jr., J. (**1980**). "X-ray diffraction study of $Zr(Ca,Y)O_{2-x}$. II. Local ionic arrangements," Acta Crystallogr., Sect. A: Cryst. Phys., Diffr., Theor. Gen. Crystallogr. **36**, 520–530.

Newville, M., Ravel, B., Haskel, D., Rehr, J. J., Stern, E. A., and Yacoby, Y. (**1995**). "Analysis of multiple-scattering XAFS data using theoretical standards," Physica B **208–209**, 154–156.

Pattanaik, S., Huffman, G. P., Sahu, S., and Lee, R. J. (**2004**). "X-ray absorption fine structure spectroscopy and X-ray diffraction study of cementitious materials derived from coal combustion by-products," Cem. Concr. Res. **34**, 1243–1249.

Peters, F., Schwarz, K., and Epple, M. (**2000**). "The structure of bone studied with synchrotron X-ray diffraction, X-ray absorption spectroscopy and thermal analysis," Thermochim. Acta **361**, 131–138.

Ressler, T. (**1998**). "*WinXAS*: A program for X-ray absorption spectroscopy data analysis under MS-Windows," J. Synchrotron Radiat. **5**, 118–122.

Rodríguez-Carvajal, J. (**1990**). "FullProf: A program for Rietveld refinement and pattern matching analysis," Satellite Meeting on Powder Diffraction of the XV Congress of the IUCr, Toulouse, France, p. 127.

Rush, G. E., Chadwick, A. V., Kosacki, I., and Anderson, H. U. (**2000**). "An EXAFS study of nanocrystalline yttrium stabilized cubic zirconia films and pure zirconia powders," J. Phys. Chem. B **104**, 9597–6906.

Silva, V. V. and Lameiras, F. S. (**2000**). "Synthesis and characterization of composite powders of partially stabilized zirconia and hydroxyapatite," Mater. Charact. **45**, 51–59.

Sowrey, F. E., Skipper, L. J., Pickup, D. M., Drake, K. O., Lin, Z., Smith, M. E., and Newport, R. J. (**2004**). "Systematic empirical analysis of calcium-oxygen coordination environment by calcium K-edge XANES," Phys. Chem. Chem. Phys. **6**, 188–192.

Stapper, G., Bernasconi, M., Nicoloso, N., and Parrinello, M. (**1999**). "*Ab initio* study of structural and electronic properties of yttria-stabilized cubic zirconia," Phys. Rev. B **59**, 797–810.

Steele, B. C. H. (**1996**). "Materials for high-temperature fuel cells," Philos. Trans. R. Soc. London, Ser. A **354**, 1695–1710.

Tolentino, H., Cezar, J. C., Cruz, D. Z., Compagnon-Cailhol, V., Tamura, E., and Martins Alves, M. C. (**1998**). "Commissioning and first results of the LNLS XAFS beamline," J. Synchrotron Radiat. **5**, 521–523.

Tommaseo, C. E., and Kersten, D. M. (**2002**). "Aqueous solubility diagrams for cementitious waste stabilization systems. 3. Mechanism of zinc immobilizaton by calcium silicate hydrate," Environ. Sci. Technol. **36**, 2919–2925.

Trovarelli, A., (Ed.) (**2002**). *Catalysis by Ceria and Related Materials* (Imperial College Press, London).

Vlaic, G., Fornasiero, P., Geremia, S., Kašpar, J., and Graziani, M. (**1997**). "Relationship between the zirconia-promoted reduction in the Rh-loaded $Ce_{0.5}Zr_{0.5}O_2$ mixed oxide and the Zr–O local structure," J. Catal. **168**, 386–392.

Vlaic, G., Monte, R. D., Fornasiero, P., Fonda, E., Kašpar, J., and Graziani, M. (**1999**). "Redox property-local structure relationships in the Rh-loaded CeO_2–ZrO_2 mixed oxides," J. Catal. **182**, 378–389.

Yaparpalvi, R., Loyalka, S. K., and Tompson, Jr., R. V. (**1994**). "Production of spherical ZrO_2–Y_2O_3 and ZnO particles," J. Biomed. Mater. Res. **28**, 1087–1093.

Yashima, M., Sasaki, S., Kakihana, M., Yamaguchi, Y., Arashi, H., and Yoshimura, M. (**1994**). "Oxygen-induced structural change of the tetragonal phase around the tetragonal-cubic phase boundary in ZrO_2–$YO_{1.5}$ solid solutions," Acta Crystallogr., Sect. B: Struct. Sci. **50**, 663–672.

Yashima, M., Kakihana, M., and Yoshimura, M. (**1996**). "Metastable-stable phase diagrams in the zirconia-containing systems utilized in solid-oxide fuel cell application," Solid State Ionics **86–88**, 1131–1149.

Yashima, M., Sasaki, S., and Yamaguchi, Y. (**1998**). "Internal distortion in ZrO_2–CeO_2 solid solutions: neutron and high-resolution synchrotron x-ray diffraction study," Appl. Phys. Lett. **72**, 182–184.

Yuren, W., Kunquan, L., Dazhi, W., Zhonghua, W., and Zhengzhi, F. (**1994**). "The EXAFS study of nanocrystalline zirconia," J. Phys.: Condens. Matter **6**, 633–640.